

Black Hole–Scalar Field Interactions in Spherical Symmetry

R. L. Marsa

*Department of Physics and Astronomy
The University of Pittsburgh
Pittsburgh, PA*

M. W. Choptuik

*Center for Relativity
The University of Texas at Austin
Austin, TX
(July 15, 1996)*

We examine the interactions of a black hole with a massless scalar field using a coordinate system which extends ingoing Eddington-Finkelstein coordinates to dynamic spherically symmetric-spacetimes. We avoid problems with the singularity by excising the region of the black hole interior to the apparent horizon. We use a second-order finite difference scheme to solve the equations. The resulting program is stable and convergent and will run forever without problems. We are able to observe quasi-normal ringing and power-law tails as well an interesting nonlinear feature.

I. INTRODUCTION

A longstanding goal of relativists has been the long-time numerical evolution of a black hole spacetime. Such an evolution is difficult because of the physical singularity the spacetime contains. Despite their early promise, it has not sufficed to use slicings (choices of time coordinate) which avoid the physical singularity. Invariably, such coordinate systems develop coordinate singularities in the vicinity of the event horizon and computationally, physical and coordinate singularities are essentially equally pathological. Many years ago, Unruh suggested that it might help to consider evolution of only the exterior of a black hole. In fact, he argued, since the black hole interior is, by definition, causally disconnected from the rest of the universe, evolution of events within the horizon constituted wasted computational effort. In the necessary absence of exact information concerning the spatial location of the event horizon at any instant during the evolution of given black hole initial data, Unruh proposed that the apparent horizon be tracked and used as an approximation to the true horizon. Thornburg developed these ideas, first in the context of generating initial data for n black holes (each of which could have arbitrary momentum and spin) [1], and then in a program of research for solving the vacuum axisymmetric Einstein equations [2,3]. However, the first clearly successful application of the black-hole excising technique in a dynamical situation came with the work of Seidel and Suen who studied spherical evolution of the vacuum (Schwarzschild) as well as a self-gravitating massless scalar field [4]. Extensions of this work are discussed in Anninos et. al. [5].

The Seidel and Suen paper is also notable for the introduction of a general technique, termed *causal differencing*, which ensures that, independently of the details of the coordinate system adopted, the difference scheme's numerical domain of dependence contains the physical domain of dependence (i.e. is causal). Alcubierre and Schutz have used a similar but somewhat more general technique which they call *causal reconnection* to treat the wave equation on an arbitrarily moving grid [6]. Scheel et. al. have recently used black hole excising in a study of gravitational collapse in Brans-Dicke gravity [7,8].

In this paper, we again use the black hole excising technique to examine the interactions of a black hole with a massless, minimally coupled scalar field in spherical symmetry. Unlike previous work, we use a *null* based slicing to get a coordinate system (ingoing Eddington-Finkelstein) which fits naturally with black hole excision (for a Schwarzschild black hole, all variables are static and non-singular (appropriately smooth) everywhere on the solution domain, and perturbations about Schwarzschild give perturbations of this behavior). Further, we introduce a modification to these coordinates which allows for easy tracking of the apparent horizon. We are able to get a second-order, convergent evolution scheme which will stably evolve forever, and which shows the expected effects of quasi-normal ringing and the power law decay of the scalar field. We also see some interesting coordinate and nonlinear effects.

The plan of the remainder of the paper is as follows. In Sec. II, and following some unpublished previous work [9,10], we define the minimally-modified ingoing Eddington-Finkelstein (MMIEF) coordinate system and derive equations of motion for the gravitational and scalar fields which are specialized to this coordinate system. This derivation is based on detailed calculations of the Einstein-Klein-Gordon equations of motion in a general spherically symmetric coordinate system [11] which

have been summarized in Appendix A. In Sec. III, we examine the issue of regularity at the origin, $r = 0$, with the principal result that use of the coordinate system must be restricted to cases where matter never reaches $r = 0$. We follow with a detailed description of our finite difference approximations in Sec. IV and a discussion of initial data in Sec. V. We discuss the convergence and stability of our difference solutions in Sec. VI—the evidence presented there suggests that the scheme can be used to carry out arbitrarily long evolutions. Various physical and coordinate effects which have emerged from our studies are discussed in sections Sec. VII–Sec. XI and we end with some concluding remarks.

We note that the programs used to generate the results described below were written in RNPL (Rapid Numerical Prototyping Language), a language designed by the authors [11]. This language allows for the easy and compact expression of time-dependent systems of partial differential equations and the rapid trial of various finite-difference techniques for solving them.

II. MINIMALLY-MODIFIED INGOING EDDINGTON-FINKELSTEIN COORDINATES

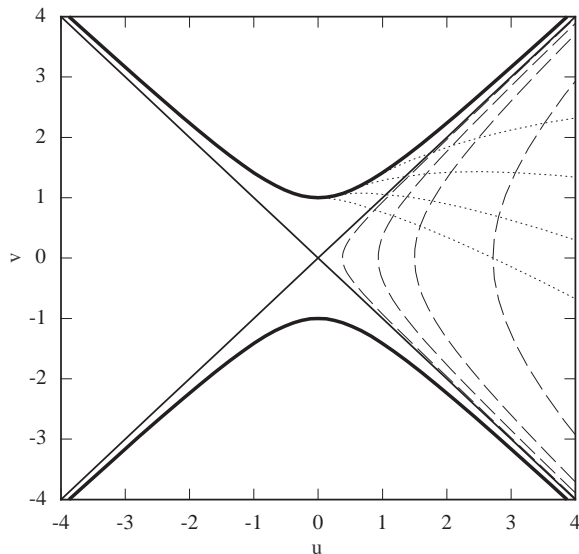


FIG. 1. The ingoing Eddington-Finkelstein slices in Kruskal-Szekeres coordinates. The dotted lines are constant t , while the dashed lines are constant r . The dark curves are the singularity. The diagonal lines are the horizon ($r = 2M$).

We begin by recalling that the ingoing Eddington-Finkelstein (IEF) coordinate system (see, for example, Chapter 30 of [12]) is defined for static, spherically-symmetric spacetimes (i.e. Schwarzschild) and combines an areal (measures proper surface area) radial coordinate r , with a time coordinate t , which is chosen so that the ingoing tangent combination $\vec{\partial}_t - \vec{\partial}_r$ is null. Fig. 1 shows some slices of constant IEF time plotted

in Kruskal-Szekeres coordinates. Notice that all of the slices penetrate the horizon and meet the singularity.

In generalizing IEF, we first consider the following general “3+1” form for a time-dependent spherically-symmetric metric:

$$ds^2 = (-\alpha^2 + a^2\beta^2) dt^2 + 2a^2\beta dt dr + a^2 dr^2 + r^2 b^2 d\Omega^2. \quad (2.1)$$

Here, a, b, α , and β are functions of r and t , and $d\Omega^2$ is the metric on the unit-sphere. We fix the spatial degree of coordinate freedom by introducing a “shifted” areal coordinate s , defined by $s \equiv r + f(t)$ for some as yet undetermined function f . With this choice, the metric becomes

$$ds^2 = (-\alpha^2 + a^2\beta^2) dt^2 + 2a^2\beta dt dr + a^2 dr^2 + s^2 d\Omega^2. \quad (2.2)$$

Comparison with the general form (A4) yields the identifications $s = rb$ and $b = 1 + f/r$. From the general evolution equation for b (A11), we have

$$(\dot{r}b) = -\alpha r b K^\theta_\theta + \beta (rb)'. \quad (2.3)$$

Here and subsequently, overdots and primes denote partial differentiation with respect to t and r respectively. Solving this last equation for the shift vector component (or simply “the shift”) β , and noting that $(\dot{r}b) = \dot{f}$, $(rb)' = 1$, we obtain the condition on the shift which must be dynamically enforced to keep the metric function s areal:

$$\beta = \dot{f} + s\alpha K^\theta_\theta. \quad (2.4)$$

We now fix the time slicing by demanding that the ingoing combination of timelike and radial tangent vectors— $\vec{\partial}_t - \vec{\partial}_r$ —be null, exactly as in the case of the original IEF coordinates. This gives a condition on the metric, namely $g_{tt} - 2g_{tr} + g_{rr} = 0$. Using (2.2) this implies

$$\alpha = \pm a(1 - \beta). \quad (2.5)$$

We choose the sign so α is positive for $\beta \leq 1$, that is $\alpha = a(1 - \beta)$. Using this and (2.4) we get

$$\beta = \frac{\dot{f} + saK^\theta_\theta}{1 + saK^\theta_\theta} \quad \alpha = \frac{a(1 - \dot{f})}{1 + saK^\theta_\theta}. \quad (2.6)$$

Hence the metric takes the form

$$ds^2 = a^2(2\beta - 1) dt^2 + 2a^2\beta dt dr + a^2 dr^2 + s^2 d\Omega^2. \quad (2.7)$$

Factoring the first three terms yields

$$ds^2 = a^2((2\beta - 1) dt + dr)(dt + dr) + s^2 d\Omega^2, \quad (2.8)$$

which shows that the characteristic speeds are

$$c = -1, 1 - 2\beta. \quad (2.9)$$

We now specialize the general spherically-symmetric equations of motion (A10)-(A18) given in Appendix A to the MMIEF coordinate system. The full set of constraint and evolution equations for the geometric variables is:

$$a' + \frac{1}{2s} (a^3 - a) + \frac{a^3 s}{2} K^\theta{}_\theta (2K^r{}_r + K^\theta{}_\theta) - 2\pi s a (\Phi^2 + \Pi^2) = 0 \quad (2.10)$$

$$K^\theta{}'_\theta + \frac{K^\theta{}_\theta - K^r{}_r}{s} - \frac{4\pi\Phi\Pi}{a} = 0 \quad (2.11)$$

$$\dot{a} = -a^2 (1 - \beta) K^r{}_r + (a\beta)' \quad (2.12)$$

$$K^\theta{}'_\theta = \beta K^\theta{}'_\theta + a(1 - \beta) K^\theta{}_\theta (K^r{}_r + 2K^\theta{}_\theta) + \frac{1 - \beta}{s^2} \left(a - \frac{1}{a} \right) + \frac{\beta'}{as} \quad (2.13)$$

$$K^r{}_r = \beta K^r{}_r + a(1 - \beta) K^r{}_r (K^r{}_r + 2K^\theta{}_\theta) + \frac{\beta - 1}{a} \left[\frac{a''}{a} - \left(\frac{a'}{a} \right)^2 - \frac{2a'}{sa} + 8\pi\Phi^2 \right] + \frac{\beta' a'}{a^2} + \frac{\beta''}{a} \quad (2.14)$$

while the wave equation for the massless scalar field becomes the first-order (in time) system:

$$\dot{\Phi} = (\beta\Phi + (1 - \beta)\Pi)' \quad (2.15)$$

$$\dot{\Pi} = \frac{1}{s^2} [s^2 (\beta\Pi + (1 - \beta)\Phi)]' - \frac{2\dot{s}}{s}\Pi. \quad (2.16)$$

We note that we have used the slicing condition, $\alpha = a(1 - \beta)$, to eliminate the lapse function from the above set. In addition, as is always the case in general relativistic dynamics, we have more constraint and evolution equations governing the geometric variables than variables themselves. We adopt the often-used (and somewhat *ad hoc*) approach of discretizing some sufficient subset of the equations with the expectation that, provided the difference scheme converges, residuals of discretized forms of the remaining equations will be of the same order in the mesh spacing as the truncation error of the difference scheme itself. In fact, we have made considerable use of our freedom to construct schemes based on various combinations of constraint and evolution equations in the development of the stable second-order methods described in Sec IV. It is entirely possible that we could construct a stable scheme without explicit use of the constraints but our attempts to do so with the type of differencing described in Sec IV were not successful.

Since the function $f(t)$ (recall $s(r, t) \equiv r + f(t)$) is still unspecified, we require one more equation to determine the time-evolution of our model system. We derive an evolution equation for f by demanding that a certain radial coordinate, $r = r_h$, be tied to the location of a marginally trapped surface. In general we will want to track the *outermost* marginally trapped surface, so in the following we will assume that the surface we are tracking is, in fact, an apparent horizon. We recall that if S^μ is an outward-pointing, space-like unit normal to a marginally trapped surface, then it satisfies [13]

$$D_i S^i - K + S^i S^j K_{ij} = 0, \quad (2.17)$$

where D_i is the covariant derivative compatible with the 3-metric and $K \equiv K^i{}_i$. In spherical symmetry, and with the functional forms of the 3-metric and extrinsic curvature given in Appendix A, this equation reduces to

$$(rb)' - arbK^\theta{}_\theta = 0. \quad (2.18)$$

In the MMIEF system this is simply

$$asK^\theta{}_\theta = 1. \quad (2.19)$$

To keep the apparent horizon at fixed r , we demand that $(as\dot{K}^\theta{}_\theta)|_{r_h} = 0$, where r_h is the initial position of the apparent horizon. Solving this equation for \dot{f} and using the constraint and evolution equations to eliminate time and space derivatives of the geometric variables, we find:

$$\dot{f} = \frac{4\pi s^2 (\Phi + \Pi)^2}{a^2} \Big|_{r_h}. \quad (2.20)$$

We are most interested in the situation where the initial data for our spacetime describes a black hole of mass M which is well separated from any scalar field. In this case we have $r_h = 2M$ and, provided that (2.20) is satisfied, the apparent horizon will remain at $r = r_h = 2M$. The area of the apparent horizon, however, is given by $4\pi s_h^2 \equiv 4\pi(r_h + f)^2$, and hence will increase as matter falls into the black hole, in accord with physical expectations.

It is useful to write down the Schwarzschild solution in IEF coordinates. The metric is usually written as [12]

$$ds^2 = - \left(1 - \frac{2M}{r} \right) d\tilde{V}^2 + 2d\tilde{V}dr + r^2 d\Omega^2, \quad (2.21)$$

where \tilde{V} is a null coordinate. Defining a time-like coordinate $t \equiv \tilde{V} - r$, the metric becomes:

$$ds^2 = - \left(1 - \frac{2M}{r} \right) dt^2 + \frac{4M}{r} dt dr + \left(1 + \frac{2M}{r} \right) dr^2 + r^2 d\Omega^2. \quad (2.22)$$

Comparison of this last result with the general form (A4) yields the following expressions for the various metric components:

$$\bar{\alpha} = \sqrt{\frac{r}{r+2M}} \quad \bar{\beta} = \frac{2M}{r+2M} \quad \bar{a} = \sqrt{\frac{r+2M}{r}}, \quad (2.23)$$

where we use overbars on quantities to stress that the expressions are valid only for the vacuum case. Using the above and equations (A10) and (A11), we can compute the extrinsic curvature components:

$$\bar{K}^\theta_\theta = \frac{2M(r+2M)}{(r(r+2M))^{\frac{3}{2}}} \quad \bar{K}^r_r = \frac{-2M(r+M)}{(r(r+2M))^{\frac{3}{2}}}. \quad (2.24)$$

Since we are working in spherical symmetry, we can meaningfully define the mass (or mass aspect) function $m(r, t)$ which, at least in a vacuum region, provides an invariant measure of the gravitational mass contained within radius r at time t . Moreover, even when matter is present, $m(r, t)$ and $m'(r, t)$ are useful diagnostic quantities in our calculations. The mass in MMIEF coordinates can be computed from the surface area using the general expression:

$$m(r, t) = \frac{1}{2}s \left(1 - (16\pi A)^{-1} A^\mu A_\mu \right), \quad (2.25)$$

where $A = 4\pi s^2$. Substituting this expression for the area into (2.25) and differentiating, we get

$$m(r, t) = \frac{1}{2}s \left(1 - \frac{1 - (s a K^\theta_\theta)^2}{a^2} \right). \quad (2.26)$$

By making use of the evolution and constraint equations, we can write this mass as an integral over the mass-density. In this form we have

$$m(r, t) = \frac{s_h}{2} + 4\pi \int_{r_h}^r s^2 \left(\frac{\Phi^2 + \Pi^2}{2a^2} + s K^\theta_\theta \frac{\Phi \Pi}{a} \right) dr, \quad (2.27)$$

where as before, r_h is the location of the apparent horizon and $s_h \equiv s(r_h)$. We note here that as used above, M represents the mass of the black hole, that is $s_h/2$. We also define M_∞ as the total mass in the spacetime, namely

$$M_\infty \equiv m(\infty) = M + 4\pi \int_{r_h}^\infty s^2 \left(\frac{\Phi^2 + \Pi^2}{2a^2} + s K^\theta_\theta \frac{\Phi \Pi}{a} \right) dr. \quad (2.28)$$

Given that our finite difference grid does not extend to infinity, we will approximate M_∞ by taking the upper limit of the above integral to be the outer boundary of our computational domain.

III. REGULARITY AT THE ORIGIN

In cases where a black hole is not initially present or there is insufficient mass in the scalar field to form a

black hole via collapse, the infalling matter will encounter the coordinate origin, $r = 0$. As is generically the case when using spherical coordinates, the various geometric and matter variables must satisfy regularity conditions as $r \rightarrow 0$ in order that the origin remain a regular point in the spacetime (see [14] for an extensive discussion of regularity conditions).

Since ϕ is a scalar and a, K^θ_θ , and K^r_r are components of rank-two tensors, we assume that they are even in r near the origin. This means that their spatial derivatives must vanish at $r = 0$:

$$\phi' = a' = K^{\theta'}_\theta = K^{r'}_r = 0. \quad (3.1)$$

Elementary flatness near the origin in MMIEF coordinates dictates that $a(0, t) = 1$. An examination of the momentum constraint (2.11) shows that $K^\theta_\theta(0, t) = K^r_r(0, t)$. We can find further conditions by examining the potentially divergent terms of the evolution equation for K^θ_θ (2.13). These terms, which are those with powers of r in the denominator, can be collected and written as

$$\frac{(1-\beta)(a^2-1) + r\beta'}{r^2 a}. \quad (3.2)$$

Clearly, as $r \rightarrow 0$ both the numerator and the denominator of (3.2) go to zero, so we use L'Hôpital's rule to compute the limit. The derivative of the numerator is $2(1-\beta)aa' - \beta'(a^2-1) + \beta' + r\beta''$. As $r \rightarrow 0$ this goes to β' . The derivative of the denominator is $r^2 a' + 2ra$. Clearly this goes to zero as r goes to zero. Thus, we must have $\beta(0, t)' = 0$.

Since we still have an indeterminate form, we apply L'Hôpital's rule again. The second derivative of the numerator is $(1-\beta)(2aa'' + 2(a')^2) - \beta''(a^2-1) - 2a\beta'a' + 2\beta'' + r\beta'''$. As r goes to zero, this goes to $2(1-\beta)a'' + 2\beta''$. The second derivative of the denominator is $r^2 a'' + 4ra' + 2a$. The limit of this is 2. Thus, we have

$$\lim_{r \rightarrow 0} \frac{(1-\beta)(a^2-1) + r\beta'}{r^2 a} = (1-\beta)a'' + \beta''. \quad (3.3)$$

Let us now consider the behavior of the spatial derivatives of β as $r \rightarrow 0$. When there is no black hole present, the shift is given by

$$\beta = \frac{raK^\theta_\theta}{1 + raK^\theta_\theta}. \quad (3.4)$$

From this we can easily see that β is zero at the origin. Now

$$\beta' = \frac{raK^{\theta'}_\theta + ra'K^\theta_\theta + aK^\theta_\theta}{(1 + raK^\theta_\theta)^2}. \quad (3.5)$$

Thus,

$$\lim_{r \rightarrow 0} \beta' = K^\theta_\theta \quad (3.6)$$

Since we have argued that $\beta'(0, t) = 0$ and $K^\theta_\theta(0, t) = K^r_r(0, t)$, we have

$$K^\theta_\theta(0, t) = K^r_r(0, t) = 0. \quad (3.7)$$

Now the second derivative of β is

$$\beta'' = \frac{raK^{\theta\theta} + 2aK^{\theta'}_\theta + 2ra'K^{\theta'}_\theta + 2a'K^\theta_\theta + ra''K^\theta_\theta}{(1 + raK^\theta_\theta)^2} - \frac{2\left((raK^\theta_\theta)'\right)^2}{(1 + raK^\theta_\theta)^3}. \quad (3.8)$$

As $r \rightarrow 0$, this expression vanishes. Thus, $\beta''(0, t) = 0$.

Since $K^\theta_\theta(0, t) = 0$, we must have $\dot{K}^\theta_\theta(0, t) = 0$ and consequently the right hand side of (2.13) must vanish as $r \rightarrow 0$. This will happen only if the limit of (3.2) is zero, which, given the results deduced above, can only happen if $a(0, t)'' = 0$.

The evolution of the scalar field is accomplished through two auxiliary variables, Φ and Π . These are defined by (A14). The condition on Φ has already been stated in (3.1)

$$\Phi(0, t) = 0, \quad (3.9)$$

and it is easy to show that Π must be even in r near the origin. Thus we have

$$\Pi'(0, t) = 0. \quad (3.10)$$

TABLE I. Two-Level Finite Difference Operators

| Operator | Definition | Expansion |
|-----------------------|---|---|
| $\Delta_r^f f_i^n$ | $(-3f_i^n + 4f_{i+1}^n - f_{i+2}^n)/2\Delta r$ | $\partial_r f_i^n + O(\Delta r^2)$ |
| $\Delta_r^b f_i^n$ | $(3f_i^n - 4f_{i-1}^n + f_{i-2}^n)/2\Delta r$ | $\partial_r f_i^n + O(\Delta r^2)$ |
| $\Delta_r f_i^n$ | $(f_{i+1}^n - f_{i-1}^n)/2\Delta r$ | $\partial_r f_i^n + O(\Delta r^2)$ |
| $\Delta_t f_i^n$ | $(f_i^{n+1} - f_i^n)/\Delta t$ | $\partial_t f_i^n + O(\Delta t^2)$ |
| $\Delta_t^d f_i^n$ | $(f_i^{n+1} - f_i^n)/\Delta t + \epsilon_{dis}[6f_i^n + f_{i-2}^n + f_{i+2}^n - 4(f_{i-1}^n + f_{i+1}^n)]/16\Delta t$ | $\partial_t f_i^n + O(\Delta t^2)$ |
| $\mu_t f_i^n$ | $(f_i^{n+1} + f_i^n)/2$ | $f_i^{n+\frac{1}{2}} + O(\Delta t^2)$ |
| $\mu_r f_i^n$ | $(f_i^n + f_{i-1}^n)/2$ | $f_{i-\frac{1}{2}}^n + O(\Delta r^2)$ |
| $\Delta_r^{fa} f_i^n$ | $\mu_t \Delta_r^f f_i^n$ | $\partial_r f_i^{n+\frac{1}{2}} + O(\Delta r^2 + \Delta t^2)$ |
| $\Delta_r^{ba} f_i^n$ | $\mu_t \Delta_r^b f_i^n$ | $\partial_r f_i^{n+\frac{1}{2}} + O(\Delta r^2 + \Delta t^2)$ |
| $\Delta_r^a f_i^n$ | $\mu_t \Delta_r f_i^n$ | $\partial_r f_i^{n+\frac{1}{2}} + O(\Delta r^2 + \Delta t^2)$ |
| $\Delta_r^s f_i^n$ | $(f_i^{n+1} - f_{i-1}^{n+1} + f_{i+1}^n - f_i^n)/2\Delta r$ | $\partial_r f_i^{n+\frac{1}{2}} + O(\Delta r^2 + \Delta t^2 + \Delta r \Delta t)$ |

Unfortunately, these regularity conditions are inconsistent with the Hamiltonian constraint (2.10). If we solve (2.10) for a' , take a radial derivative of the resulting expression, then take the $r \rightarrow 0$ limit, we find:

$$a''(0, t) \propto \Pi(0, t)^2 \neq 0. \quad (3.11)$$

Thus, we are lead to the conclusion that the MMIEF coordinate system will admit no non-singular curvature at the origin. The only consistent solutions near the origin describe flat space or a black hole. Thus, MMIEF is a “good” coordinate system to use only when a black hole already exists in the spacetime. In a spacetime without a black hole, the equations will remain consistent as long as no matter encounters the origin. This will be the case if the scalar field is outgoing or if it collapses to form a black hole before it encounters the origin. For a collapse problem, we could start with another coordinate system and change to MMIEF coordinates if an apparent horizon forms. If no such horizon forms, there is really no need for the special horizon tracking properties of MMIEF coordinates anyway. Though we have not implemented such a scheme, this approach was used successfully in [4,5,7,8].

IV. FINITE DIFFERENCE EQUATIONS

We use equations (2.12), (2.13), (2.15), (2.16), and (2.20) to evolve a , K^θ_θ , Φ , Π , and f ; equation (2.11) to find K^r_r ; and equation (2.6) to find β . We solve these equations using finite difference techniques on a uniform mesh with spacings Δr and $\Delta t = \lambda \Delta r$, where the Courant factor λ , is held fixed when we change the basic scale of discretization.

Table I shows the operators we use in the discretizations. Note that while the derivative operators take a lower precedence than the arithmetic operators, that is $\Delta_r f_i^{n^2} = (f_{i+1}^{n^2} - f_{i-1}^{n^2})/\Delta r$, the time averaging operator takes a higher precedence, that is $\mu_t f_i^{n^2} = (\mu_t f_i^n)^2$ and $\mu_t (a_i^n b_i^n) = \mu_t a_i^n \mu_t b_i^n$.

In the interior, the finite difference equations are:

$$\Delta_t^d a_i^n = -\mu_t (a^2 (1 - \beta))_i^n + \Delta_r^s (a\beta)_i^n, \quad (4.1)$$

$$\Delta_t^d K^\theta_\theta_i^n = \mu_t \beta_i^n \Delta_r^s K^\theta_\theta_i^n + \mu_t \left(\frac{1 - \beta}{s^2} \left(a - \frac{1}{a} \right) \right)_i^n + \frac{\Delta_r^a \beta_i^n}{\mu_t (as)_i^n} + \mu_t (a(1 - \beta) K^\theta_\theta (2K^\theta_\theta + K^r_r))_i^n, \quad (4.2)$$

$$\mu_t \left(\Delta_r K^\theta_\theta + \frac{K^\theta_\theta - K^r_r}{s} - 4\pi \frac{\Phi \Pi}{a} \right)_i^n = 0, \quad (4.3)$$

$$\Delta_t^d \Phi_i^n = \Delta_r^s (\beta \Phi + (1 - \beta) \Pi)_i^n, \quad (4.4)$$

$$\begin{aligned} \Delta_t^d \Pi_i^n &= \frac{1}{\mu_t (s_i^n)^2} \Delta_r^s (s^2 (\beta \Pi + (1 - \beta) \Phi))_i^n \\ &\quad - 2 \Delta_t s_i^n \mu_t \left(\frac{\Phi}{s} \right)_i^n, \end{aligned} \quad (4.5)$$

$$\Delta_t f_i^n = 4\pi \mu_t \left(\frac{s(\Phi + \Pi)}{a} \right)_i^{n2}, \quad (4.6)$$

$$s_i^{n+1} = r_i + f_i^{n+1}, \quad (4.7)$$

$$\mu_t \beta_i^n = \frac{\Delta_t f_i^n + \mu_t (asK^\theta)_i^n}{1 + \mu_t (asK^\theta)_i^n}. \quad (4.8)$$

These equations are applied everywhere in the interior except at the two points next to the boundary points. At these points, we use the same equations except the dissipative time derivatives (Δ_t^d) are replaced by regular time derivatives (Δ_t), since the value at $i+2$ or $i-2$ is not available at these locations. It is interesting to note that all of the spatial derivatives are *angled* (Δ_r^s) except for the derivative of β in equation (4.2) and the derivative of K^θ in equation (4.3). Switching any of these derivatives from angled to non-angled or from non-angled to angled results in an instability. We don't have an explanation for why this particular combination of derivatives works, but the use of angled derivatives here was motivated by their successful application in previous work by Choptuik (see [13] and [15]). This is a good example of a technique that was perfected by "experimental" numerical analysis.

As discussed previously, the inner boundary of our computational domain is fixed to the apparent horizon, $r = r_h$. In accord with the causal properties of the apparent horizon, function values on the horizon can be advanced without use of any information defined at $r < r_h$. Therefore, at $r = r_h$ we use the same equations employed in the interior, except that we replace centered differences with forward differences. For example, equation (4.1) becomes

$$\Delta_t a_i^n = -\mu_t (a^2 (1 - \beta))_i^n + \Delta_r^s (a\beta)_i^n. \quad (4.9)$$

Since the computational grid does not extend to infinity. We adopt outgoing conditions at the outer boundary, that is, we assume that no radiation will enter the grid from large r . While this is not strictly true (there will be curvature back-scattering from the outgoing pulse), this assumption provides a reasonable computational solution.

For the scalar field variables Φ and Π , the outgoing conditions come from the condition on ϕ , namely $s\phi \sim F(s - ct)$, with $c = 1 - 2\beta$ being the speed of the outgoing waves. This means that

$$\begin{aligned} \dot{\Phi} + (1 - 2\beta) \Phi' + \frac{\dot{s} + 1 - 2\beta - 2s\beta'}{s} \Phi \\ - \frac{\dot{s} + 1 - 2\beta + 2s\beta'}{s^2} \phi = 0 \end{aligned} \quad (4.10)$$

and

$$(1 - \beta) (\Pi + \Phi) + \frac{1 - 2\beta + \dot{s}}{s} \phi = 0. \quad (4.11)$$

These equations are discretized as

$$\begin{aligned} \Delta_t \Phi_i^n + (1 - 2\mu_t \beta_i^n) \Delta_r^b \Phi_i^n \\ + \frac{\Delta_t s_i^n + 1 - 2\mu_t \beta_i^n - 2\mu_t s_i^n \Delta_r^b \beta_i^n}{\mu_t s_i^n} \mu_t \Phi_i^n \\ - \frac{\Delta_t s_i^n + 1 - 2\mu_t \beta_i^n + 2\mu_t s_i^n \Delta_r^b \beta_i^n}{(\mu_t s_i^n)^2} \mu_t \phi_i^n = 0 \end{aligned} \quad (4.12)$$

and

$$\mu_t [(1 - \beta) (\Phi + \Pi)]_i^n + \frac{1 - 2\mu_t \beta_i^n + \Delta_t s_i^n}{\mu_t s_i^n} \mu_t \phi_i^n = 0. \quad (4.13)$$

We can get approximate conditions on a and K^θ from their Schwarzschild forms (2.23) and (2.24) with the mass aspect (2.27) used in place of M , since in vacuum, or in any region where the scalar field's self-gravitation is negligible, a and K^θ should take on these forms. For large s , asymptotic expansion of these expressions gives:

$$a \sim 1 + \frac{m(r, t)}{s} + O(s^{-2}) \quad (4.14)$$

and

$$K^\theta \sim \frac{2m(r, t)}{s^2} + O(s^{-3}). \quad (4.15)$$

Thus, at large s we have, to leading order

$$s(a - 1) \sim m(r, t) \quad (4.16)$$

and

$$s^2 K^\theta \sim m(r, t). \quad (4.17)$$

We now deduce how $m(r, t)$ behaves in the large s , weak-field limit. Since $a \rightarrow 1$ and $K^\theta \rightarrow 0$ we have

$$m \sim 4\pi \int s^2 (\Phi^2 + \Pi^2) ds. \quad (4.18)$$

From the condition on ϕ we can see that $\Phi \sim G(u)/s$ and $\Pi \sim G(u)/s$, where $u \equiv s - ct$. Thus

$$m \sim 8\pi \int G^2(u) du \sim H(u), \quad (4.19)$$

that is, m is "outgoing" at large s . Therefore we get the following conditions for a and K^θ :

$$s(a - 1) \sim H(s - ct) \quad (4.20)$$

and

$$s^2 K^\theta \sim H(s - ct). \quad (4.21)$$

These are discretized as

$$\Delta_t (s(a-1))_i^n + (1 - 2\mu_t \beta_i^n) \Delta_r^{ba} (s(a-1))_i^n = 0 \quad (4.22)$$

and

$$\Delta_t (s^2 K^\theta)_i^n + (1 - 2\mu_t \beta_i^n) \Delta_r^{ba} (s^2 K^\theta)_i^n = 0. \quad (4.23)$$

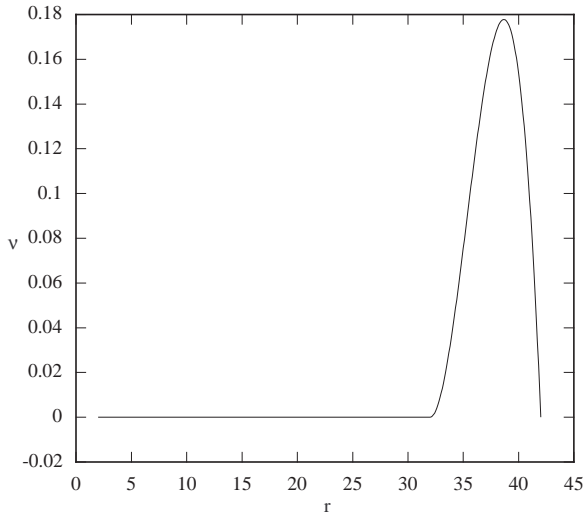


FIG. 2. Sponge filter coefficient function for $A = 1.0$ and $n = 2$.

The outgoing boundary condition reduces the amplitude of reflections off the boundary, but unless the boundary is placed at very large r , these reflections can still interfere with the results of a calculation. To further reduce the reflections, we use a *sponge filter* as detailed in [13]. Briefly, this means that in the interior of the grid, we add a term to the wave equation which effectively applies the outgoing condition on a finite region rather than at a single radial location. For instance, we use the following modified evolution equation for Φ :

$$\begin{aligned} \dot{\Phi} = & (\beta\Phi + (1-\beta)\Pi)' \\ & - \nu \left[\dot{\Phi} + (1-2\beta)\Phi' + \frac{\dot{s} + 1 - 2\beta - 2s\beta'}{s}\Phi \right. \\ & \left. - \frac{\dot{s} + 1 - 2\beta + 2s\beta'}{s^2}\phi \right], \end{aligned} \quad (4.24)$$

where the coefficient function, $\nu(r)$, is given by

$$\nu(r) = A \frac{(r-r_s)^n (r_{max}-r)}{(r_{max}-r_s)^{n+2}} (n+1)(n+2)$$

in the filtering region, $r_s \leq r \leq r_{max}$, and vanishes elsewhere. Here, A and n are parameters which can be adjusted to tune the filter. Fig. 2 shows ν for $A = 1.0$ and $n = 2$, the values used in this work.

V. INITIAL DATA

We wish to examine the interactions of the black hole with compact ingoing pulses of scalar field. We can generate nearly ingoing pulses using the following method. Let $\phi(r, t) = F(u \equiv r + t)/r$. This gives $\dot{\phi} = \partial_u F/r$ and $\phi' = \partial_u F/r - F/r^2$. For a compact pulse, we set F to a Gaussian of the form

$$F(u) = Au^2 \exp\left(-\frac{(u-c)^d}{\sigma^d}\right), \quad (5.1)$$

where d is an integer, and c is the radial coordinate of the center of the pulse. This results in scalar field initial data of the form

$$\phi = Ar \exp\left(-\frac{(r-c)^d}{\sigma^d}\right) \quad (5.2)$$

$$\Phi = \phi \left[\frac{1}{r} - \frac{d(r-c)^{d-1}}{\sigma^d} \right] \quad (5.3)$$

$$\Pi = \phi \left[\frac{2-\beta}{r(1-\beta)} - \frac{d(r-c)^{d-1}}{\sigma^d} \right]. \quad (5.4)$$

We solve for β, a , and K^θ_θ using equations (2.6), (2.10), and (2.11). Ostensibly, $K^r_r(0, r)$ can be freely specified and the constraints can still be satisfied by appropriate adjustments to the other geometric variables. However, an *arbitrarily* chosen $K^r_r(0, r)$ combined with the initial data for the scalar field given by (5.2)–(5.4) will not, in general, generate a spacetime describing the desired physical scenario of a scalar pulse initially infalling on a black hole. We therefore adopt an ansatz for $K^r_r(0, r)$ which is motivated by the observation that at the initial time, the self-gravitation of the scalar field is generally relatively weak, and thus the geometric variables should have approximately their Schwarzschild form. Specifically, we demand that $K^r_r(0, r)$ satisfy the following equation (see (2.24)):

$$K^r_r = \frac{-2m(r+m)}{(r(r+2m))^{\frac{3}{2}}}, \quad (5.5)$$

where m is the mass aspect function defined by (2.27). This equation, along with the equation for the mass aspect (2.27) and the constraints (2.10) and (2.11), is then solved iteratively for any given initial scalar field configuration. We have found that initial data prepared in this manner *does* generate spacetimes of the type we seek even when the scalar field is significantly self-gravitating at the initial time.

VI. CONVERGENCE AND STABILITY

In order to assess the correctness and accuracy of our difference equations and the program which solves

them, we perform some tests. These include computing convergence factors, performing a long-time vacuum (Schwarzschild) evolution and comparing it to the known solution, and performing a long-time strong-field evolution.

To measure convergence, we define the convergence factor for a grid function u by

$$C_f \equiv \frac{|\hat{u}_{2h} - \hat{u}_{4h}|_2}{|\hat{u}_h - \hat{u}_{2h}|_2}, \quad (6.1)$$

where \hat{u}_α is a solution of the finite difference equations on a grid with spacing α , and the ℓ_2 norm is defined in the usual way, that is

$$|\hat{u}|_2 \equiv \sqrt{\frac{\sum_{i=1}^N u_i^2}{N}}. \quad (6.2)$$

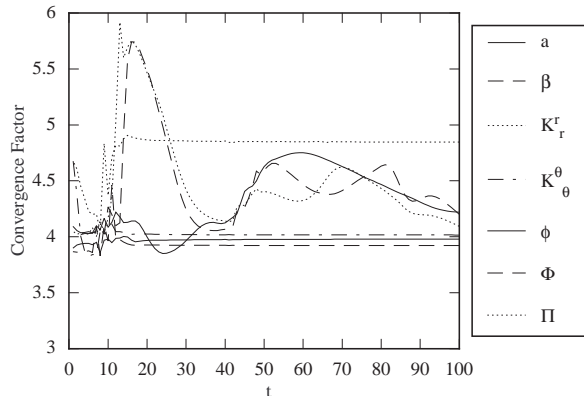


FIG. 3. Convergence factors as a function of time for a strong-field evolution with $A = 2.5 \times 10^{-3}$, $c = 10$, and $\sigma = 2$. These values are approximately four, indicating second order convergence.

The convergence factors for the scalar field and geometric variables are shown in Fig. 3. These factors are computed from a strong-field evolution. They are approximately four throughout, indicating second order convergence.

Fig. 4 shows the deviation of the evolved vacuum spacetime from that of Schwarzschild. We note however, that the spacetime being evolved is not Schwarzschild, rather it is a black hole in a “box” with rather *ad hoc* boundary conditions.

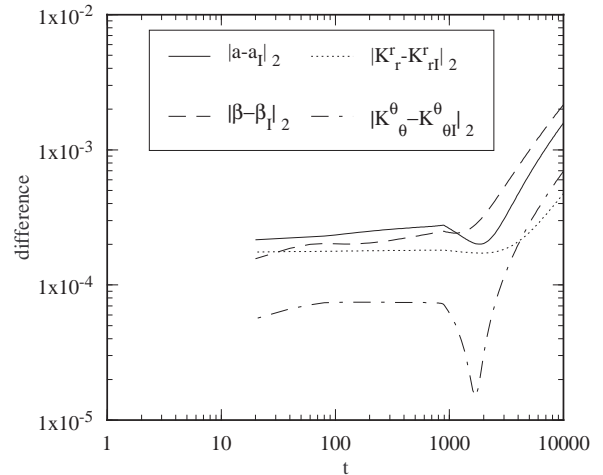


FIG. 4. The ℓ_2 norms of the differences of the computed vacuum geometrical variables and their Schwarzschild values versus time. Note that both axes are logarithmic. The outer boundary for this evolution was placed at $r = 82M$.

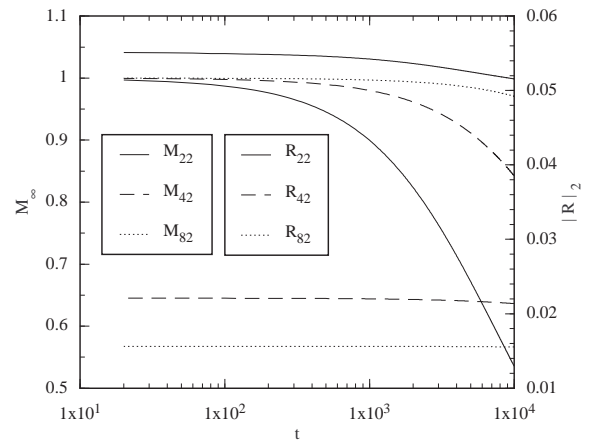


FIG. 5. The mass and the ℓ_2 norm of the 4-Ricci scalar for vacuum spaces with varying outer boundary position. The subscripts indicate the position of the outer boundary in units of M . The time axis is logarithmic.

At late times, the outer boundary condition causes the spacetime to “drift” away from the initial configuration. Fig. 5 shows plots of the mass and the Ricci scalar for vacuum evolutions with outer boundaries at $22M$, $42M$, and $82M$. This plot clearly shows the rather large effect the position of the outer boundary has on the late-time evolution. We could get better convergence of the difference solution to the continuum solution (i.e. with boundary conditions only at spatial infinity) by matching the interior Cauchy evolution to an exterior characteristic evolution (see [16,17]) or by using an adaptive mesh refinement algorithm to push the the outer boundary to a large radius without unduly increasing the computational load. Nevertheless, the position of the outer boundary has no effect on stability. This can be seen clearly in Fig. 6. The curves in this graph are asymptoting to fixed values. Thus, although the computed spacetime drifts from

Schwarzschild, it eventually reaches a fixed configuration.

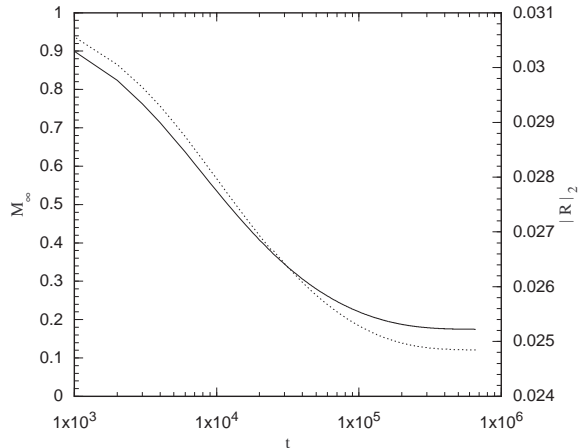


FIG. 6. The mass (solid line) and the ℓ_2 norm of the 4-Ricci scalar (dotted line) for a vacuum evolution with outer boundary at $r = 22M$. Both functions are asymptoting to a fixed value, indicating that the spacetime is settling down to a static configuration. The time axis is logarithmic.

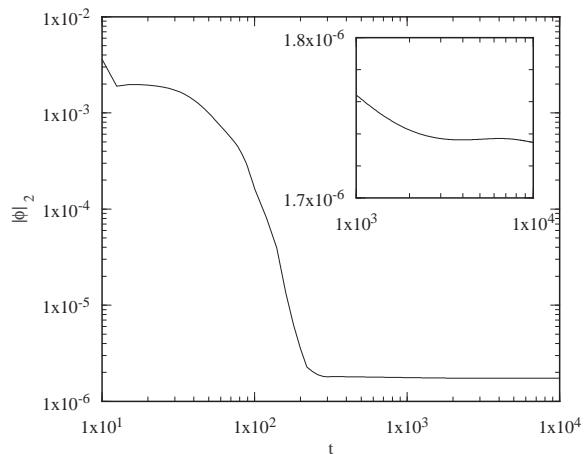


FIG. 7. A log-log plot of the ℓ_2 norm of the scalar field versus time for a strong-field evolution. The inset shows an expanded vertical axis for the late time evolution. The outer boundary is at $r = 42M$.

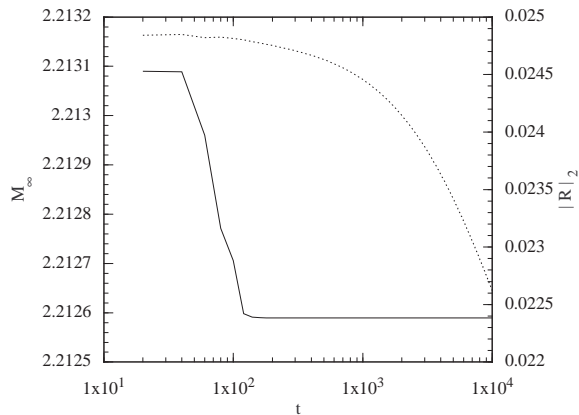


FIG. 8. The mass (solid line) and the ℓ_2 norm of the 4-Ricci scalar (dotted line) versus time for a strong-field evolution. The mass should be nearly constant except for a small amount of scalar field which radiates to infinity. The plot of the Ricci scalar shows the drifting of the geometry caused by the outer boundary conditions. Contrary to the impression given by this figure, the Ricci scalar is asymptoting to a fixed value. The time axis is logarithmic.

Fig. 7 shows the ℓ_2 norm of the scalar field during a strong field evolution to $t = 10000M$. Fig. 8 shows the mass and the Ricci scalar for the same evolution. While the scalar field and the mass fall off as expected, the plot of the Ricci scalar again shows the “drifting” of the geometry.

The plots of the Ricci scalar were made by discretizing to first order, the analytic expression for R derived in the usual way by $R = R^\mu{}_\mu$, where $R_{\mu\nu}$ is the Ricci tensor. Although the values of R appear large given that they are computed for a vacuum spacetime, they do converge to zero to first order in the mesh spacing as expected. Moreover, the values of the individual additive terms in the expression for R are orders of magnitude larger than the scalar itself, indicating that R is the size we would expect for first order differencing at these resolutions.

VII. MASS SCALING

As discussed in Sec. V we focus study on the evolution of initially ingoing “Gaussian” pulses of scalar radiation. In this case, the infalling field exhibits two limiting behaviors, dependent on the amplitude and width of the pulse. These are: *scattering* from the existing black hole and *collapse* to form a new horizon outside the existing horizon. Generically, these two behaviors are separated by a *critical* value of either amplitude or width. Fig. 9 shows the path of the apparent horizon for various amplitudes of initial data.

The final mass of the black hole should scale as a power of the amplitude of the initial pulse. To find out what this power should be, we can use equation (2.28). Since the mass is conserved, M_∞ is a constant. However, M is not constant. As the scalar field encounters the horizon, some mass will be transferred from the integral term to M . The mass of the black hole will increase by an amount proportional to the mass in the scalar field. By this we mean that after the interaction we have

$$M \rightarrow M + 4\pi k \int_{r_h}^{\infty} s^2 \left(\frac{\Phi^2 + \Pi^2}{2a^2} + sK^\theta{}_\theta \frac{\Phi\Pi}{a} \right) dr, \quad (7.1)$$

where k is a positive constant less than 1. For a very narrow pulse, the entire mass of the field will go into the black hole, and hence, k will be very close to 1. If the pulse is very wide, however, k will be very close to 0. Thus, to see how the final mass of the black hole scales with the amplitude of the scalar pulse, we need only examine the integral term in equation (7.1).

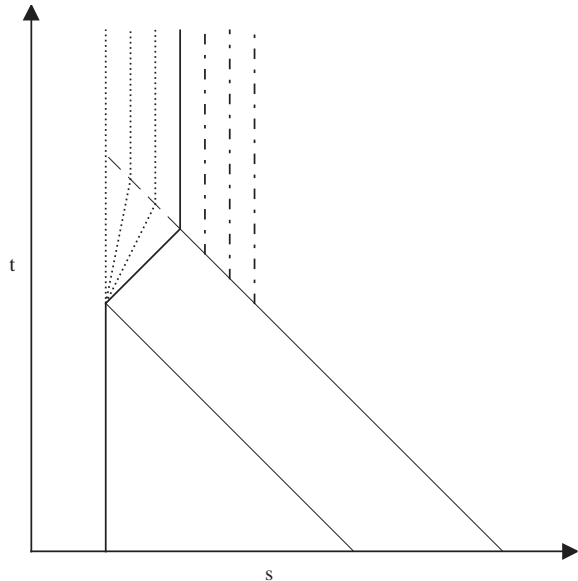


FIG. 9. Schematic motion of the horizon for various amplitudes of the scalar field. Notice that this diagram uses the areal coordinate s and not the radial coordinate r . The solid dark vertical line which jogs right and then continues vertically represents the critical path of the horizon. The dotted lines are sub-critical paths and the vertical dashed lines are super-critical paths. The two thin, diagonal lines represent the bounds of the ingoing pulse of scalar field. A super-critical pulse moves inward until it crosses its gravitational radius. Once this happens, the apparent horizon jumps from its initial position to this new position where it remains. A sub-critical pulse moves inward until it encounters the horizon. If the field is very weak, the horizon is unaffected. For stronger fields, the horizon moves out until the pulse is entirely inside. For a critical pulse, the horizon moves out at the speed of light. Note however, that unless the energy density is a square wave, the horizon will not move along the straight lines as shown in the diagram, but will move along a curve with gradually increasing and then decreasing slope.

From equations (5.2)-(5.4) we see that Φ and Π are proportional to ϕ and hence to A . This means that the integrand is proportional to A^2 . This of course assumes the dependence of a , K^θ_θ , and β on ϕ is much less than the dependence of $m(r)$ on ϕ . While this seems a reasonable assumption, it must be checked numerically in the strong field regime.

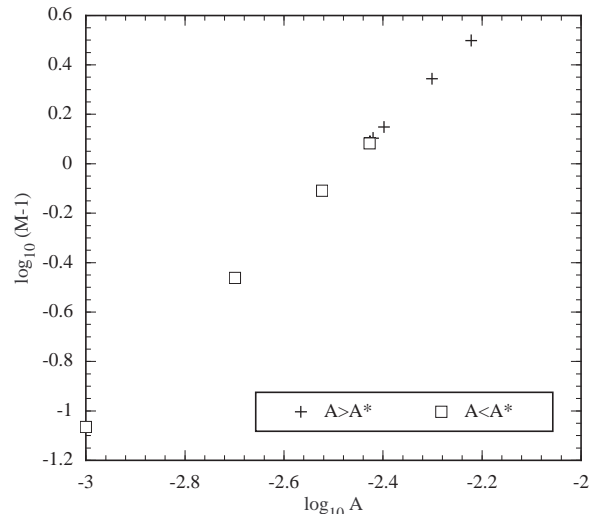


FIG. 10. A log-log plot of the final black hole mass versus the amplitude of the scalar field pulse for initial data with $d = 2$, $\sigma = 2$, and $c = 10$. The squares represent data with amplitude less than the critical value, while the crosses represent data with amplitude greater than the critical value. The slope of this line is 2.01 showing that the black hole mass depends on the square of the scalar field amplitude.

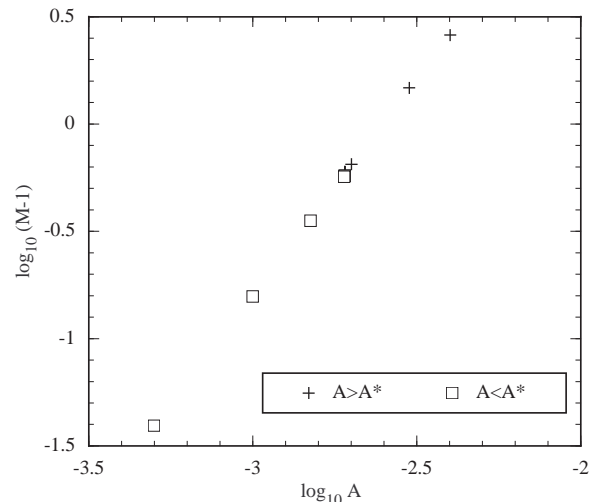


FIG. 11. A log-log plot of the final black hole mass versus the amplitude of the scalar field pulse for initial data with $d = 4$, $\sigma = 2$, and $c = 10$. The slope of this line is 1.99 indicating again that the black hole mass depends on the square of the scalar field amplitude.

Our numerical results verify this calculation. For instance, the data in Fig. 10 is fit by the line

$$\log(M - 1) = 2.01 \log A + 4.96, \quad (7.2)$$

indicating that the mass grows with the square of the amplitude as expected. The graph also shows there is no difference in behavior for sub- and super-critical data. That is, the final mass of the black hole exhibits the same dependence on the amplitude when the hole grows by accretion as when it forms by collapse.

Similarly, the data in Fig. 11 is fit by the line

$$\log(M - 1) = 1.99 \log A + 5.19, \quad (7.3)$$

indicating that the mass scaling is independent of the exact shape of the ingoing pulse.

VIII. TAILS

Fig. 12 shows ϕ at constant r for runs with $r_{max} = 42, 82, 162$. It is clear that the position of the outer boundary has a large effect on the late-time fall-off of the scalar field. Even with the sponge filter, there is enough reflection from the outer boundary to cause the field to die off more slowly than it otherwise would.

However, with the outer boundary at $r_{max} = 162$, it takes at least $300M$ for reflections from the scattered pulse to travel in from the outer boundary and interfere with measurements at $r = 30$, and still longer for reflections to interfere with measurements at the horizon. This should provide enough time to accurately measure the rate of fall-off of the scalar field. Fig. 13 shows the evolution of ϕ at $r = 30$ and at the horizon up until $t = 300M$. A fit to the $r = 30$ curve between $200M$ and $300M$ shows ϕ falling off as $t^{-3.38}$. A fit to the horizon curve over the same range shows ϕ falling off as $t^{-3.06}$.

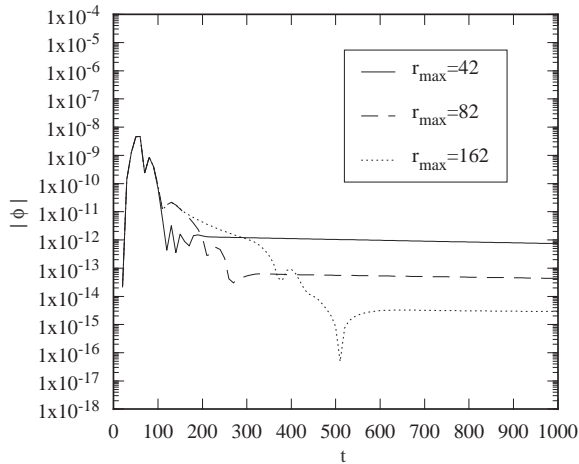


FIG. 12. The absolute value of the scalar field at $r = 30M$ versus time for various spatial domains. Notice the differences in late time fall off caused by the different positions of the outer boundary. The vertical axis is logarithmic.

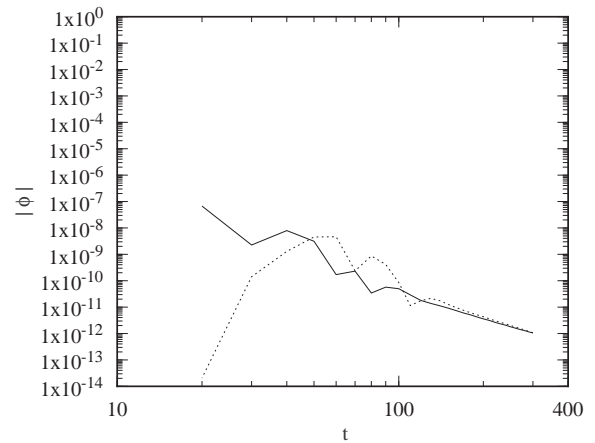


FIG. 13. A log-log plot of the absolute value of the scalar field at the horizon (solid line) and at $r = 30M$ (dotted line) versus time for an evolution with the outer boundary at $r = 162M$.

Linearized perturbation theory predicts these exponents should both be -3 [18]. We note that previous evolutions carried out by Gundlach, Price, and Pullin gave exponents between -2.63 and -2.74 for ϕ at constant r [19].

IX. RINGING

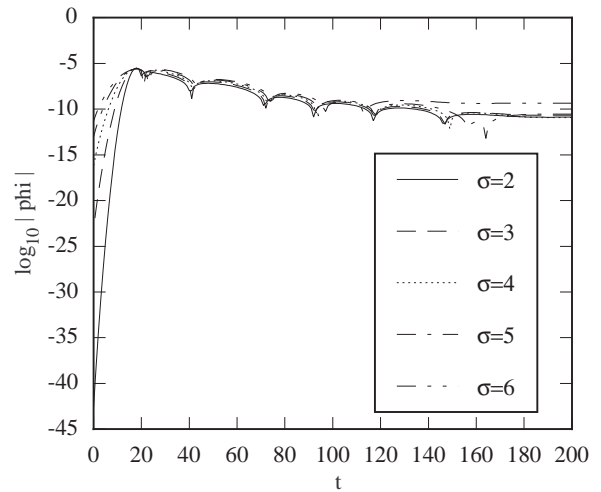


FIG. 14. $\log |\phi|$ at the horizon versus time for various pulse widths ($A = 2.0 \times 10^{-8}$). While the curves match well for about $100M$, there are differences in late-time behavior exhibited by the wider pulses, particularly those with $\sigma = 5$ and $\sigma = 6$. This is an outer boundary effect. As the width becomes larger, less and less of the initial pulse is absorbed by the black hole. This means there is more scalar field available to be reflected from the outer boundary and this causes differences in the late-time evolution.

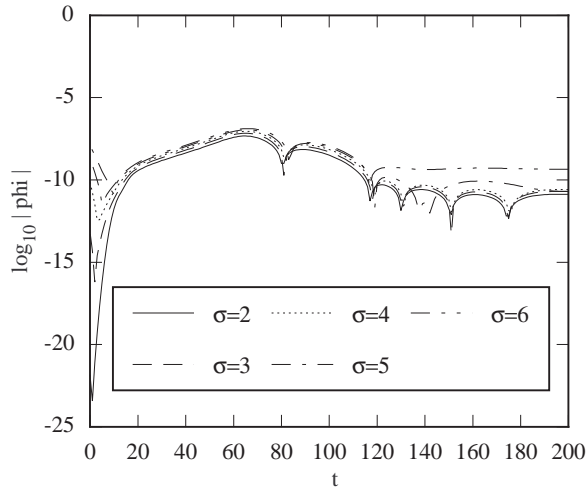


FIG. 15. $\log |\phi|$ at $r = 30$ verses time for various pulse widths ($A = 2.0 \times 10^{-8}$).

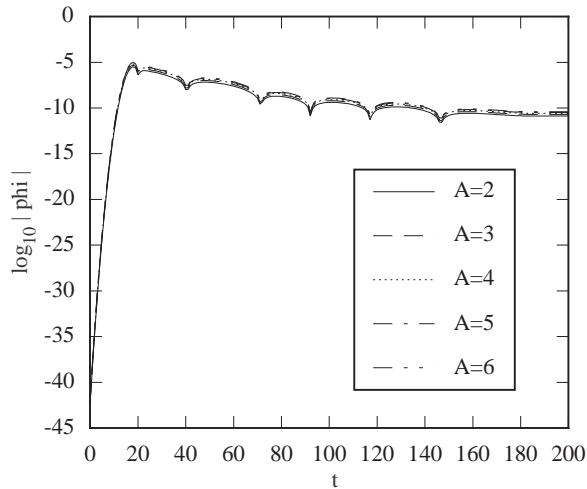


FIG. 16. $\log |\phi|$ at the horizon verses time for various pulse amplitudes ($\sigma = 2.0$, amplitudes are $\times 10^{-8}$).

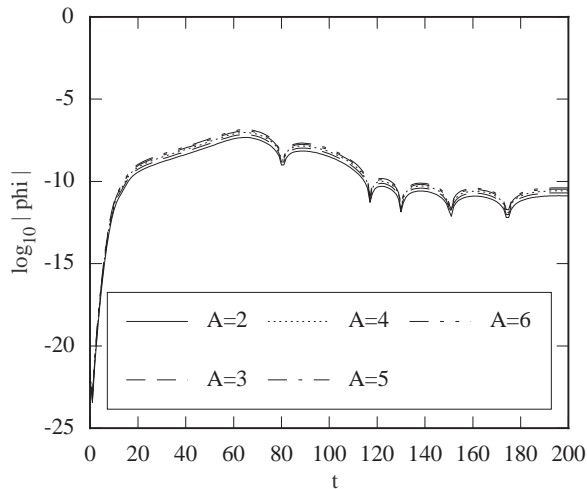


FIG. 17. $\log |\phi|$ at $r = 30$ verses time for various pulse amplitudes ($\sigma = 2.0$, amplitudes are $\times 10^{-8}$).

Figs. 14-17 show the waveforms generated by the scattering of packets of various widths and amplitudes. The scalar field is measured both at the horizon and at $r = 30M$. The oscillation period in each of these figures is approximately $53M$, and is independent of initial amplitude and pulse width. Gundlach *et. al.* measured an oscillation period of approximately $47M$ [19] during collapse of Gaussian wave packets.

X. COORDINATE EFFECTS

Certain evolutions exhibit interesting effects which result from the use of MMIEF coordinates. Recall that the shift component, β satisfies (2.6). At the apparent horizon, (2.19) holds so we have

$$\beta(r_h, t) = \frac{f(t)}{2} + \frac{1}{2}. \quad (10.1)$$

From this we can see that when no matter is crossing the horizon, $\beta = 1/2$ so the outgoing characteristic speed (2.9) is zero, as it must be since the tracked surface is marginally trapped. However, if $\dot{f} = 1$, then $\beta = 1$ and the outgoing characteristic speed is -1 . In this case, the light cone is degenerate. In fact, from (2.6) we can see that if $\dot{f} = 1$, then $\beta = 1$ *everywhere*. Does \dot{f} ever equal one? The most likely place for this to happen is the critical solution because that is when the “maximum” amount of energy is crossing the horizon for a given pulse shape. The values of β at the horizon and at the outer boundary are plotted in Fig. 18 for a near-critical solution. β gets as large as .95, but never reaches 1. A near-critical solution from a family of pulses with $d = 4$ gives a slightly higher maximum β , but still less than 1. It may be possible that a narrow enough pulse could cause \dot{f} to reach 1 for an instant, but this has not been verified. Furthermore, it may be that such a narrow pulse would collapse to form a new horizon before crossing the existing horizon.

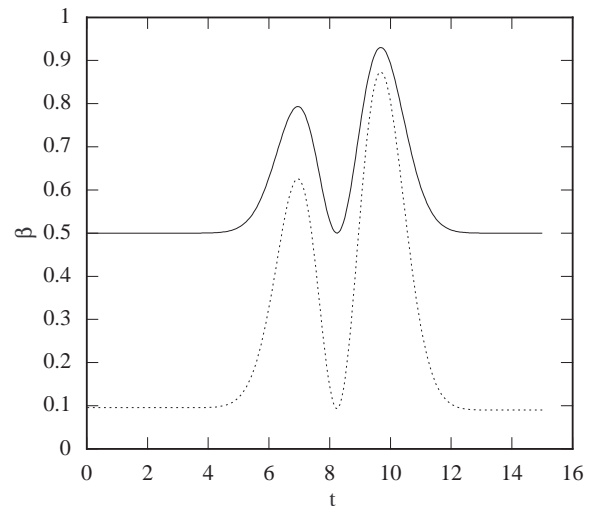


FIG. 18. β at the horizon (solid line) and the outer boundary (dotted line) for a near-critical solution with $\sigma = 2, d = 2,$ and $c = 10$. The outer boundary is at $r = 42M$. Outgoing pulses of scalar radiation will exhibit retrograde motion whenever $\beta > .5$.

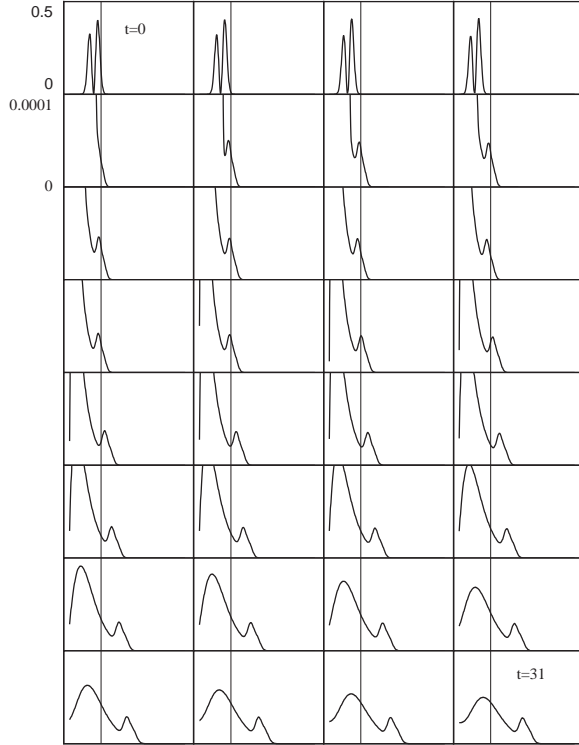


FIG. 19. Evolution of m' for a near-critical solution with $\sigma = 2, d = 2,$ and $c = 10$. Retrograde motion is apparent near $t = 7M$ and $t = 10M$. The frames are spaced $1M$ apart in time. The vertical scale changes at $t = 5M$ so that the small outgoing pulse can be observed. The thin vertical lines passing through the frames provide a common horizontal reference to aid detection of the retrograde motion.

Nevertheless, whenever $\beta > .5$, the outgoing characteristic speed is negative. Thus, outgoing pulses will appear to move inward when plotted in the radial coordinate, r . Fig. 19 shows an evolution of m' for the critical solution described above. There are two periods of backwards motion; one at about $7M$ and the other at about $10M$. These are the times when each of the “bumps” crosses the horizon. The retrograde motion is easier to see in Fig. 20 which shows contours of m' on a spacetime plot for the same evolution. Fig. 21 shows a fairly weak field evolution of m' for comparison. There is no retrograde motion in this case.

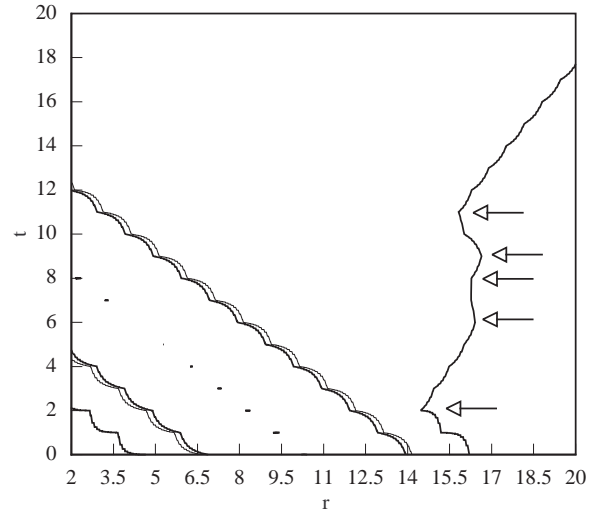


FIG. 20. Contour plot of m' for a near-critical solution with $\sigma = 2, d = 2,$ and $c = 10$. The small pulse moves out between the first and second arrows then moves back in between the second and third arrows. It then moves out briefly between the third and fourth arrows and then moves back in between the fourth and fifth arrows before renewing its outward motion.

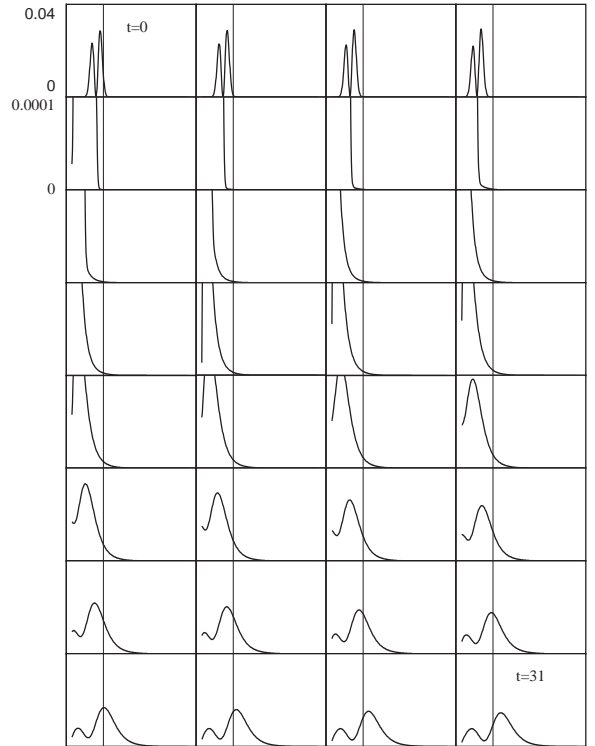


FIG. 21. Evolution of m' for a weak-field solution with $A = .001, \sigma = 2, d = 2,$ and $c = 10$. The frames are spaced $1M$ apart in time. The vertical scale changes at $t = 5M$ the small outgoing pulses can be observed. There is no retrograde motion apparent.

To completely remove these coordinate motion effects, we can abandon the shifted areal coordinate s and use

the usual IEF coordinates. In this case, r is areal again so $b = 1$ instead of $1 + f/r$. The evolution and constraint equations are trivially derived from equations (2.10)-(2.16) with the substitutions $s \rightarrow r$ and $\dot{s} \rightarrow 0$. Note that the function $f(t)$ no longer appears.

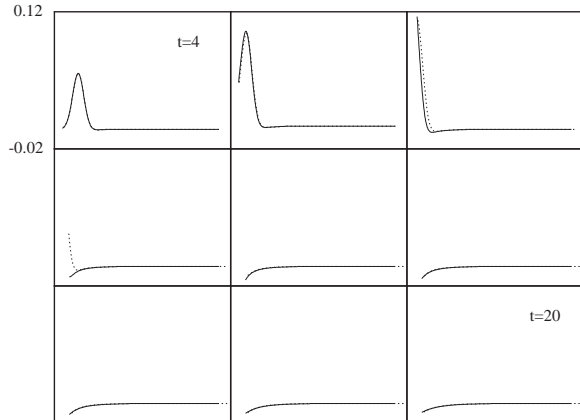


FIG. 22. A comparison of ϕ computed in IEF coordinates (solid line) compared with ϕ computed in MMIEF coordinates (dotted line). The frames are spaced $2M$ in time. The horizontal axis extends from 0 to $45M$ in areal radius. Differences between the two computations are caused by small differences in the position of the inner boundary.

Such a coordinate choice has the additional benefit of slightly simplifying the equations. However, the inner boundary of the grid will not be tied to the apparent horizon as it is in MMIEF coordinates. This causes no problems in practice. As matter crosses the horizon and the black hole grows, some of the inner grid points are “lost” into the black hole and we simply stop applying our difference equations there. Since the radial coordinate is areal, the growth of the black hole is bounded by the total mass of the spacetime, so there is no danger of having a large fraction of the grid fall into the hole. The previous one-dimensional black hole excising calculations [4,5,7,8] used horizon-locked radial coordinates so that once the apparent horizon formed, no further grid points would fall into the hole. Thus, they should be expected to exhibit similar coordinate motion effects to those seen in the calculations using MMIEF coordinates.

Fig. 22 shows a comparison of ϕ evolved in IEF coordinates with ϕ evolved in MMIEF coordinates for a strong-field case. The two match closely with differences caused by small differences in the positions of the inner boundary.

XI. NONLINEAR EFFECTS

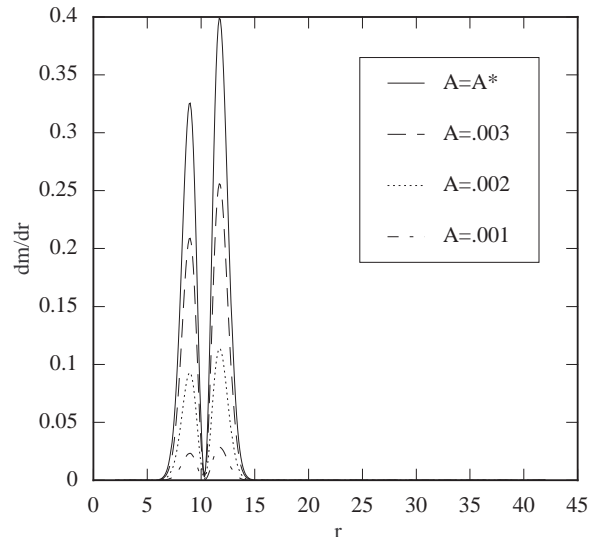


FIG. 23. m' at $t = 0$ for $\sigma = 2$, $d = 2$, $c = 10$, and various amplitudes, including near-critical (A^*).

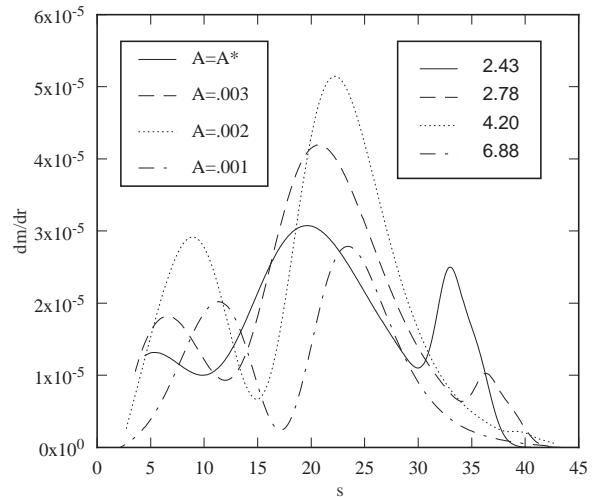


FIG. 24. m' at $t = 40M$ for $\sigma = 2$, $d = 2$, $c = 10$, and various amplitudes. The inset shows 1000 times fraction of mass scattered. For instance, the near-critical solution has .243 percent of its mass scattered.

There is a sharp “bump” at the front of the outgoing pulse in Fig. 19. This feature is absent from the weak-field evolution of Fig. 21 and is certainly amplitude dependent. Fig. 23 shows a series of initial pulse shapes for data with various amplitudes all centered at $r = 10$. Fig. 24 shows the corresponding pulse shapes after scattering.

Although this bump occurs at the front of the scattered pulse, it is not caused by interactions with the black hole. To see this more clearly, we can start the pulse further out and see what happens. Figs. 25 and 26 show pulse shapes at $t = 0$ and $t = 8$ for data with $c = 20$. The outgoing

bump develops for large amplitude data without any help from the black hole. A similar bump develops for initial data with $d = 4$. These bumps always have the same characteristic shape, though their widths may vary.

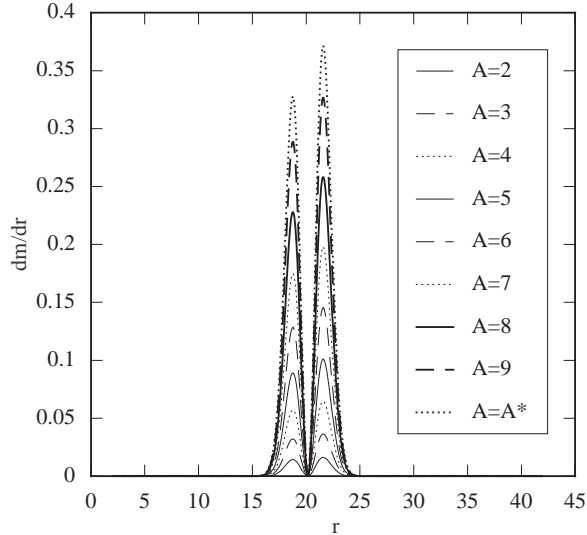


FIG. 25. m' at $t = 0$ for $\sigma = 2$, $d = 2$, $c = 20$, and various amplitudes ($\times 10^{-4}$).

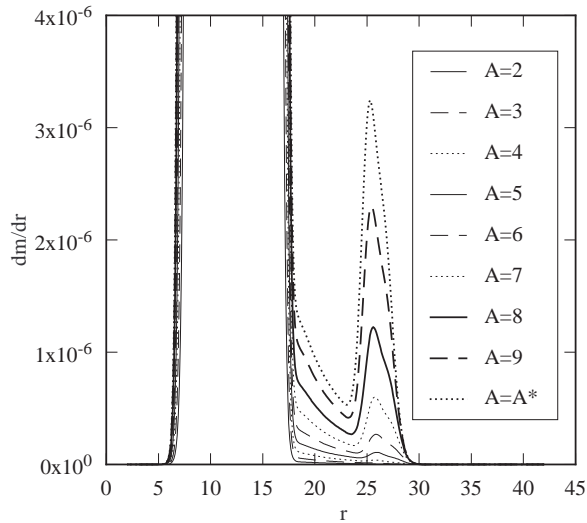


FIG. 26. M' at $t = 8$ for $\sigma = 2$, $d = 2$, $c = 20$, and various amplitudes ($\times 10^{-4}$). The small outgoing pulse appears before scattering with the black hole.

It is clear from Fig. 24 that the amplitude of this outgoing feature does not depend linearly on the initial amplitude of the pulse. For instance, from Fig. 23, the height of the highest peak is about 1.5 times the height of the next highest peak, while their widths are the same. However, the amplitude of the outgoing feature in the first case is about 2.5 times the amplitude of the outgoing feature in the second case, while their widths are the same. Figures 25 and 26 show similar nonlinear behavior for the pulses centered at $r = 20$. It is difficult to tell

whether this feature is caused by the nonlinear interaction of an outgoing piece of the initial data with the rest of the pulse, or if it is caused by back-scattering from the effective self-potential of the ingoing pulse. Further study is needed.

XII. CONCLUSIONS

We have shown that the a *null* based slicing works well with an apparent horizon boundary condition, and results in a program which is stable and convergent and will run forever. Further, we have examined the coordinate motion effects which result from this coordinate system and ways to avoid them. We have also seen an interesting nonlinear feature in the self-gravitating scalar field.

While the calculations presented in this paper were carried out in spherical symmetry, the coordinate system can be generalized to multi-dimensions. We have worked out an extension to the case of a Kerr black hole in 3 dimensions (see [11]), the details of which will be presented elsewhere.

Unfortunately, this coordinate system can not be applied globally to spacetimes which contain more than one black hole since it depends on the notion of an areal coordinate. Nevertheless, this technique is useful for problems involving various matter fields and single black holes. For instance, it could be used to investigate the stability properties of the solution found by Bechmann and Lechtenfeld [20] in their investigation of the scalar no-hair theorem (see [11] for work in this direction).

ACKNOWLEDGMENTS

This work was supported in part by the Texas Advanced Research Project TARP-085 to Richard Matzner, the Cray Research Grant to Richard Matzner, NSF PHY9318152 (ARPA supplemented) to the Grand Challenge Alliance, and NSF PHY9510895 to the University of Pittsburgh. Most of this work was done at the University of Texas at Austin as part of [11].

It is MWC's pleasure to thank W.G. Unruh for his contributions to the early stages of this research and particularly for the suggestion that the Eddington-Finkelstein coordinate system could be extended through the introduction of the shifted areal coordinate, s .

APPENDIX: SPHERICALLY SYMMETRIC EINSTEIN-KLEIN-GORDON EQUATIONS

In spherical symmetry (using the usual spherical coordinate names (t, r, θ, ϕ) , the three-metric h_{ij} and the extrinsic curvature tensor K^i_j are diagonal. We have

$$h_{ij} = \text{diag} (a^2(t, r), r^2 b^2(t, r), r^2 b^2 \sin^2 \theta) \quad (\text{A1})$$

$$K^i_j = \text{diag} (K^r_r(t, r), K^\theta_\theta(t, r), K^\theta_\theta) \quad (\text{A2})$$

$$\beta^i = (\beta(t, r), 0, 0) \quad \alpha = \alpha(t, r) \quad \phi = \phi(t, r) \quad (\text{A3})$$

$$ds^2 = (-\alpha^2 + a^2\beta^2) dt^2 + 2a^2\beta dt dr + a^2 dr^2 + r^2 b^2 d\Omega^2. \quad (\text{A4})$$

The nonzero components of the Christoffel symbols are:

$$\Gamma^r_{rr} = \frac{\partial_r a}{a} \quad \Gamma^r_{\theta\theta} = -\frac{rb\partial_r(rb)}{a^2} \quad \Gamma^\theta_{r\theta} = \frac{\partial_r(rb)}{rb} \quad (\text{A5})$$

$$\Gamma^r_{\phi\phi} = -\sin^2\theta \frac{rb\partial_r(rb)}{a^2} \quad \Gamma^\phi_{r\phi} = \frac{\partial_r(rb)}{rb} \quad (\text{A6})$$

$$\Gamma^\theta_{\phi\phi} = -\sin\theta \cos\theta \quad \Gamma^\phi_{\phi\theta} = -\cot\theta \quad (\text{A7})$$

The two non-zero components of the Ricci tensor are

$$R^r_r = -\frac{2}{arb} \partial_r \frac{\partial_r(rb)}{a} \quad (\text{A8})$$

$$R^\theta_\theta = \frac{1}{ar^2b^2} \left[a - \partial_r \left(\frac{rb}{a} \partial_r(rb) \right) \right]. \quad (\text{A9})$$

The evolution equations for the metric components are

$$\dot{a} = -a\alpha K^r_r + (a\beta)' \quad (\text{A10})$$

$$\dot{b} = -\alpha b K^\theta_\theta + \frac{\beta}{r} (r\beta)'. \quad (\text{A11})$$

The evolution equations for the components of the extrinsic curvature are

$$\begin{aligned} \dot{K}^r_r &= \beta K^{r'}_r + \alpha K^r_r K - \frac{1}{a} \left(\frac{\alpha'}{a} \right)' \\ &\quad - \frac{2\alpha}{arb} \left[\frac{(rb)'}{a} \right]' - \pi\alpha \frac{\Phi^2}{a^2} \end{aligned} \quad (\text{A12})$$

$$\dot{K}^\theta_\theta = \beta K^{\theta'}_\theta + \alpha K^\theta_\theta K + \frac{\alpha}{(rb)^2} - \frac{1}{a(rb)^2} \left(\frac{\alpha rb}{a} (rb)' \right)'. \quad (\text{A13})$$

The massless Klein-Gordon equation is formulated in terms of the two auxiliary fields Φ and Π which are defined by

$$\Phi \equiv \phi' \quad \Pi \equiv \frac{\alpha}{a} (\dot{\phi} - \beta\phi') \quad (\text{A14})$$

With these variables, the Klein-Gordon equation is

$$\dot{\Phi} = \left(\beta\Phi + \frac{\alpha}{a}\Pi \right)' \quad (\text{A15})$$

$$\dot{\Pi} = \frac{1}{r^2b^2} \left[r^2b^2 \left(\beta\Pi + \frac{\alpha}{a}\Phi \right) \right]' - 2\Pi \frac{\dot{b}}{b}. \quad (\text{A16})$$

The Hamiltonian constraint is

$$\begin{aligned} & -\frac{2}{arb} \left[\left(\frac{(rb)'}{a} \right)' + \frac{1}{rb} \left(\left(\frac{rb}{a} (rb)' \right)' - a \right) \right] \\ & + 4K^r_r K^\theta_\theta + 2K^{\theta 2}_\theta = 8\pi \left(\frac{\Phi^2 + \Pi^2}{a^2} \right) \end{aligned} \quad (\text{A17})$$

and the momentum constraint is

$$\frac{(rb)'}{rb} (K^\theta_\theta - K^r_r) - K^{\theta'}_\theta = -4\pi \frac{\Phi\Pi}{a}. \quad (\text{A18})$$

-
- [1] Thornburg, J., M.Sc. Thesis, University of British Columbia (1985).
 - [2] Thornburg, J., *Class Quant Grav* **4**, 1119–1131 (1987).
 - [3] Thornburg, J., Ph.D. Thesis, University of British Columbia (1993).
 - [4] Seidel, E. and W. Suen., *Phys Rev Let* **69**, 1845–1848 (1992).
 - [5] Anninos, P. et. al., *Phys Rev D* **51** 5562–5578 (1995).
 - [6] Alcubierre, M. and B. F. Schutz, *J Comp Phys* **112**, 44–77 (1994).
 - [7] Scheel, M.A. et. al., *Phys Rev D* **51**, 4208–4235 (1995).
 - [8] Scheel, M.A. et. al., *Phys Rev D* **51**, 4236–4249 (1995).
 - [9] Choptuik, M. W. and W. G. Unruh. Unpublished Work (1988).
 - [10] Choptuik, M. W., Unpublished Notes (1989).
 - [11] Marsa, R. L., Ph.D. Thesis, University of Texas at Austin (1995).
 - [12] Misner, C. W. et. al., *Gravitation*. (1973).
 - [13] Choptuik, M. W., Ph.D. Thesis, University of British Columbia (1986).
 - [14] Bardeen, J. M. and T. Piran, *Phys Rep* **96**, 205–250 (1983).
 - [15] Choptuik, M. W., *Phys Rev D* **44**, 3124–3135 (1991).
 - [16] Bishop, N. T. et. al., *Phys Rev Let* **76**, 4303–4307 (1996).
 - [17] Gomez, R. et. al., “Cauchy-characteristic Evolution of Einstein-Klein-Gordon Systems.” to appear in *Phys Rev D* (1996).
 - [18] Gundlach, C. et. al., *Phys Rev D* **49**, 883–889 (1994).
 - [19] Gundlach, C. et. al., *Phys Rev D* **49**, 890–899 (1994).
 - [20] Bechmann, O. and O. Lechtenfeld, *Class Quant Grav* **12**, 1473–81 (1995).